Arabian Journal of Chemistry (2022) **15**, 104382

King Saud University

Arabian Journal of Chemistry

www.ksu.edu.sa
www.sciencedirect.com

ORIGINAL ARTICLE

Green synthesis of loofah-based biosorbent via radiation grafting for effective removal of methylene blue

Yuan Zhao [a,b], Tao Chen [b], Xiao-Fang Song [a], Jin-Yu Yang [a], Ya-Yang Wang [a], Yue-Sheng Li [b,*], Yi Liu [a,c,*]

[a] *Key Laboratory of Coal Conversion and New Carbon Materials of Hubei Province & Institute of Advanced Materials and Nanotechnology, School of Chemistry, Wuhan University of Science and Technology, Wuhan 430081, PR China*
[b] *Hubei Key Laboratory of Radiation Chemistry and Functional Materials, Hubei University of Science and Technology, Xianning, Hubei 437100, PR China*
[c] *State Key Laboratory of Separation Membrane and Membrane Process, College of Chemistry, Tiangong University, Tianjin 300387, PR China*

Received 14 July 2022; accepted 20 October 2022
Available online 27 October 2022

KEYWORDS

Adsorption;
Electron beam irradiation;
Loofah sponge;
Methylene blue;
Sodium 4-vinylbenzene sulfonate

Abstract A new loofah-based biosorbent with high adsorption capacity for cationic dye was synthesized by a one-step co-radiation grafting method. The successful grafting of sodium 4-vinylbenzene sulfonate (SSS) onto loofah sponge (LFs) through electron beam radiation can significantly improve the remove capacity of methylene blue in wastewater. The biosorbent with a 409.67 mg/g of uptake capacity for methylene blue (MB), was higher than most of the loofah based adsorbents reported. FT-IR, elemental analysis, XRD, SEM and TG were used to analyze the changes in the functional group composition, element content, morphology, thermal stability of the obtained biosorbent. The pH, contact time, temperature and the effect of dosage on adsorption were also investigated. The results showed that the adsorption behavior well accorded with the pseudo-second-order kinetic and Langmuir adsorption model, which proved that the adsorption was a single-layered and chemisorption process. The thermodynamic parameters suggested a spontaneous and endothermic process. XPS analysis confirmed a potential adsorption mechanism was based on hydrogen bond interaction, electrostatic interaction and π-π stacking. Additionally, the adsorbent owned outstanding reusability, which could be reused five times with a slight reduction of removal rate. Overall, this research enriches the MB trapping agent and provides a new methods

* Corresponding authors.
E-mail addresses: frank78929@163.com (Y.-S. Li), yiliuchem@whu.edu.cn (Y. Liu).
Peer review under responsibility of King Saud University.

Production and hosting by Elsevier

https://doi.org/10.1016/j.arabjc.2022.104382

for the reuse of waste natural loofah sponge, and it will be a valuable research with the advantages of low cost and less environmental pollution.

1. Introduction

Water is an important resource for our survival and plays a vital role in living environment (Li et al., 2018). However, industrialization activities have led to large amounts of water contaminants discharged into the global water system. This inevitably leads to the serious depletion of clean water resources. (Oun et al., 2021; Aldahash et al., 2022; Anastopoulos and Pashalidis, 2019; Liang et al., 2020). Therefore, the elimination of biological, inorganic, and organic contaminants from waste water is of great importance.

With rapid industrial development, dyes are being extensively used in food additives, textiles, cosmetics, as well as synthetic fields (Nnaji et al., 2020; Li et al., 2019). However, the overuse of dyes has lead to numerous environmental problems and human health problems (Xu et al., 2018). The dye-containing wastewater could reduce the transparency of water bodies, rendering the survival of aquatic animals and plants difficult (Mu et al., 2022). In humans, the ingestion of dyes can severely damage the digestive, nervous, and liver systems (Schio et al., 2021a). Especially cationic dyes can easily interact with negatively charged cells on membrane surfaces within body and enter into cells. This situation causes some health problems (Duman et al., 2015).

Several approaches, such as membrane filtration, biological decomposition, catalytic degradation, chemical oxidation and adsorption, have been proposed for mitigating dye-containing pollutants in wastewater treatment processes (Tunc et al., 2013; Alizadeh et al., 2022; Zhao et al., 2018; Gautam et al., 2020; Schio et al., 2021b). Among these approaches, the adsorption separation method was considered to be one of the most promising dye-containing wastewater treatment processes because of its low cost, high-efficiency, and simplicity (Han et al., 2022; Hassanzadeh-Afruzi et al., 2022; Mehdizadeh et al., 2022; Akter et al., 2022).

Conventional adsorbents, such as activated carbon, used in dye-containing wastewater treatment processes, exhibited enormous carbon footprint during the synthesis and application processes (Tshikovhi et al., 2020). Therefore, environment-friendly and cost-effective adsorbent with low carbon footprint and excellent performance should be developed for sustainable use (Sakhiya et al., 2021).

Biomass exhibited tremendous potential as sustainable resource for cleaning dye-containing wastewater (Mohammed et al., 2018). Loofah sponge (LFs) is an inexpensive and renewable natural resource (Siddiqui et al., 2018; Khadir et al., 2020a) that mainly contains lignin, cellulose, and hemicellulose (Liatsou et al., 2017). LFs were vascular bundles with a network-like structure and were typically cultivated as a commercial crop in many countries (Mallampati et al., 2015). Compared with other woody biomass, LFs exhibit unique porous physical structure and excellent mechanical properties (Su et al., 2018a) and were widely used in adsorbents (Su et al., 2018b). For example, LFs-based composite adsorption materials have been used in the adsorption of oily pollutants (Alvarado-Gómez et al., 2021), dye wastewater (Nnaji et al., 2021), radioactive Uranium (VI) (Feng et al., 2021), and heavy metal ions (Adewuyi and Pereira, 2017).

Generally speaking, raw LFs exhibited a low adsorption capacity (Anastopoulos and Pashalidis, 2020). Therefore, preparing functionalized biosobent by grafting functional monomers on the cellulose skeleton of LFs is crucial for realizing effective dye absorption in wastewater (Gedam and Dongre, 2016). Furthermore, the chemical structure and surface charge of loofah sponge limit its cationic dye removal efficiency. To overcome these problems, grafting-modification techniques have attracted considerable research attention (Chen et al., 2021). Among numerous modification methods, radiation grafting is a mild, high-efficiency, and environmentally friendly technique (Zhao et al., 2021; Du et al., 2020) for preparing high-efficiency adsorbents (Du et al., 2021; Hong et al., 2019). In this research, the loofah-based functional biosorbent was prepared through radiation grafting technique and investigated the adsorption performance of environmental pollutants.

Sodium 4-styrene sulfonate (SSS) is a kind of strong anion electrolyte, which can be as functional monomer to constitute grafted functional polymer. SSS had been grafted to magnetic chitosan in our previous study to uptake dyes (Chen et al., 2021). However, its adsorption capacity is only 126.4 mg/g. Following our ongoing interest in "green chemistry" for high concentration dye removal, a biosorbent was prepared by PSSS grafted on the surface of LFs through radiation grafting technique.

In this study, a facile, green and sustainable biosorbent was firstly prepared through a one-step method via electron beam radiation. The adsorption capacity was tested with cationic MB. Moreover, Considering multiple factors, this study conducted various experiments to optimize adsorption conditions for MB uptake. Firstly, the absorbed dose and concentration of the sodium 4-vinylbenzene sulfonate were investigated. Then the impacts of initial concentration of MB, pH, temperature, contact time, adsorption isotherms, kinetics, thermodynamics, regeneration performance and possible mechanisms were evaluated. Results showed that the LFs-PSSS exhibited superior adsorption capacity towards MB than most of the reported loofah based adsorbent.

2. Experimental section

2.1. Materials

LFs were obtained from a local luffa field (Hubei, China), and sodium 4-vinylbenzene sulfonate (SSS, purity > 90 %) was supplied by Bide Pharmaceutical Technology Co., ltd (Shanghai, China). Analytically pure MB (purity > 98 %), rhodamine B (purity > 98 %), Congo red, methyl orange (purity > 96 %), hydrochloric acid (HCl, 36.0 ~ 38.0 %), anhydrous ethanol (≥99.5 %), and sodium hydroxide (NaOH, ≥ 96 %) were obtained from Sinopharm Chemical Reagent Co. ltd (Shanghai, China). The ultrapure water (18.25MΩ·cm) were used throughout the experiments.

2.1.1. Pretreatment of LFs

Alkali-activated LFs were prepared according to the following steps. Firstly, LFs were cut into even pieces of dimensions 2 × 2 cm. Subsequently, LFs were repeatedly scrubbed with clean water to remove adhering dirt. After drying for 5 h under 333.15 K and cooling natural. The LFs were poured into 5 % (W/W) NaOH solution at 323.15 K for 3 h under continuous stirring to remove lignin and enhance the hydrophilicity (Su et al., 2018a). Finally, the LFs fibers were separated and washed to stable pH with ultrapure water, then followed by 5 h drying at 333.15 K for subsequent use.

2.1.2. Preparation of LFs-PSSS

LFs-PSSS were prepared as follows: first, 2.0 g alkali-activated LFs were accurately weighed and added to the plastic bag, and

the bag was vacuum sealed to remove air. Next, 60 mL 20 % (w/w) sodium 4-vinylbenzene sulphonate (SSS) solution was nitrogen purged for 15 min to remove dissolved oxygen. Then, the obtained SSS solution was added into plastic bag by syringe. The sealed reaction system was subjected to irradiation under an electron accelerator (1 MeV, Wasik Associates, USA) at 20 kGy/pass (range, 20–240 kGy) at normal pressure and temperature conditions (Chen et al., 2021). After irradiation, samples were filtered and washed by ultrapure water and anhydrous ethanol for several times, until all monomers and homopolymer were removed. Next, the samples were dried at 323.15 K for subsequent use. The route of LFs-PSSS preparation is illustrated in Scheme 1.

The grafting yield (GY) of LFs was calculated as follows Eqs. (1):

$$GY(\%) = \frac{W_g - W_0}{W_0} \times 100\% \quad (1)$$

Where W_0 (g) and W_g(g) are the weight of LFs and LFs-PSSS, respectively.

2.2. Characterization of LFs-PSSS

The X-ray photoelectron spectroscopic (XPS) was characterized by a PHI5300 photoelectron spectroscopic (Thermo Fisher Scientific, America), the binding energies were calibrated using the C 1 s as a reference (C 1 s = 284.6 eV). Fourier transform infrared (FT-IR) spectra was conducted via a NICOLET 5700 spectrometer (Thermo Fisher Nicolet, America) by using KBr as back ground ranging from 4000 to 400 cm^{-1}. The element contents was determined by a elemental analyzer (Vario EL Cube, Germany). The morphology was measured via a S-4800 scan electron microscopy (Hitachi, Japan). The thermogravimetry analysis (TGA) was observed by TG 209F3 (NETZSCH, Germany) under N_2 atmosphere with a heating rate of 10 °C min^{-1} between 30 and 700 °C. The differential scanning calorimetry (DSC) was performed by DSC200F3 (NETZSCH, Germany). Zeta potential was measured by 90Plus PALS (Brookhaven, America). X-ray powder diffraction (XRD) was performed on a LabX XRD-6100 (Shimadzu, Japan).

2.3. Adsorption tests

The MB adsorption performance of LFs-PSSS was evaluated through a serious of batch adsorption tests. The adsorption properties were investigated using 20 mL MB as a model dye at room temperature, and the optimal dosage for MB uptake was considered to be 1.0 g/L LFs-PSSS. To explore the influence of pH on the uptake capacity, the pH value of MB varied from 2.0 to 12.0, and 0.1 M NaOH or 0.1 M HCl was used to adjust the pH of MB solution. The MB concentration at 664 nm was determined using a UV–vis spectrophotometer (UV1901).

For evaluating adsorption kinetic data, kinetics studies of MB (MB solution concentration 100–400 mg/L) sorption onto LFs-PSSS were performed at various agitation times with other parameters unchanged (pH = 7.0, T = 298.15 K). Adsorption isotherm studies were conducted under diverse original MB solution concentrations (range, 50–600 mg/L) at 298.15, 308.15, and 318.15 K (pH = 7.0, t = 360 min).

Each adsorption assay was conducted in duplicate to ensure accuracy, Eqs. (2–4) were used to calculate the dye uptake capacities (Q, mg/g) and the removal rate (R, %) of the MB solution, respectively:

$$Q_t = \frac{(C_0 - C_t)V}{m} \quad (2)$$

$$Q_e = \frac{(C_0 - C_e)V}{m} \quad (3)$$

$$R(\%) = \frac{C_0 - C_t}{C_0} \times 100\% \quad (4)$$

Where Q_t and Q_e represent the adsorption capacity of LFs-PSSS for methylene blue at time t and equilibrium adsorption capacity, respectively (mg/g). Furthermore, C_0, C_t, and C_e represent the original MB solution concentration before adsorption, the remaining MB solution concentration at a given time, and the MB solution's equilibrium concentration, respectively (mg/L). Here, m (mg) and V (mL) denote adsorbent weight and MB solution volume, respectively, and R (%) represents the removal ratio of the MB solution by LFs-PSSS after the adsorption was completed.

Scheme 1 Schematic of LFs-PSSS preparation by using electron beam radiation.

3. Results and discussion

3.1. Characterizations of LFs-PSSS

Fig. 1 displays the FT-IR spectra of LFs and LFs-PSSS. As demonstrated in these spectra, the potent and multiple vibration peak of approximately 3423 cm^{-1} reflected that O—H existed within the polysaccharide fraction of LFs (Su et al., 2018a). Strong vibration peaks were observed from the spectra of LFs-PSSS at 3014 and 2942 cm^{-1}, which were related to the stretching vibration of absorption peaks of hydrocarbons within methyl and methylene. Compared to LFs, several novel bands were observed form LFs-PSSS. Peaks observed at 1059 and 1145 cm^{-1} could be linked with the $-SO_3^-$ group.

After grafting with PSSS, benzene ring bending vibration was appeared at 761 cm^{-1}. Furthermore, the typical benzene ring skeleton vibration absorption was detected at 1456, 1490 and 1636 cm^{-1}; Besides, the bands detected at 847 and 907 cm^{-1} were associated with the *para*-substitution of the benzene ring (Chen et al., 2021; Gao et al., 2017; Babaei et al., 2019). The appearance of the stretching vibration peaks of C═C, the characteristic of benzene ring absorption, and S group confirmed that LFs have been successfully modified with PSSS through electron beam irradiation.

Elemental analysis (EA) is commonly used to determine the elemental composition of materials. As showed in Table S1, the carbon, nitrogen and sulfur content in LFs is lower than raw-LFs. Especially, the contents of nitrogen and sulfur decreased obviously after alkalization treatment, which was attributed to the removal of lignin, proteins, flavonoids, gums and other hydrophobic compounds on the surface of LFs (Su et al., 2018b). A further decrease in nitrogen content and increase in carbon and hydrogen content indicates that SSS was successfully grafted onto the LFs surface.

XRD patterns for LFs, LFs-PSSS, and LFs-PSSS-MB are presented in Fig S1. The results demonstrate that the XRD pattern of the LFs, LFs-PSSS, and LFs-PSSS-MB were all exhibited broad peaks, which represented the features of amorphous substances. The broad peaks were observed around 16° and 22° was attribute to the amorphous structure of LFs. (Schio et al., 2021b).

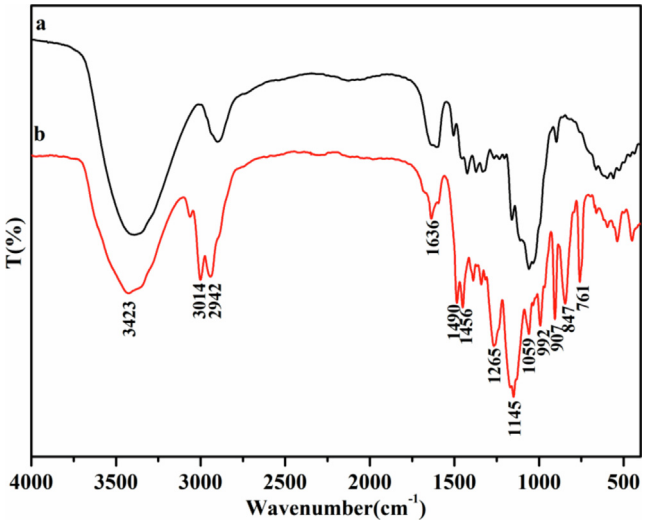

Fig. 1 FT-IR spectra of LFs (a) and LFs-PSSS (b).

The peaks of LFs-PSSS shifted to 17° and 22° and the relative intensities decreased due to the grafting of sodium 4-vinylbenzene sulfonate. This infers that grafting has resulted in the decrease in the peak intensity of grafted sample. It has been observed that the incorporation of sodium 4-vinylbenzene sulfonate to the backbone impaired the crystallinity of the fiber. (Gupta et al., 2013) Therefore, on grafting, percentage crystallinity decreases with reduction in stiffness and hardness. For LFs-PSSS and LFs-PSSS-MB, the LFs peak overlapped with others. During the adsorption process, the disorder arrangement of amorphous materials was considered positive because of more adsorption sites (Schio et al., 2021a).

Fig. 2 displays the morphology of raw-LFs, LFs and LFs-PSSS. It is obviously observed that the surface of the raw-LFs is very rough, and even some flaky impurities were attached to the loofah fibers. Notably, after alkali treatment, LFs fibers reveal that a multi-directional array forms mat-like morphology,and small holes, cracks as well as ravine-like fissures were exist on the fiber surface, which is highly conducive for adsorbents within water solution. (Khadir et al., 2020b). This rough structure can effectively increase the specific surface area of loofah and facilitate surface modification. After grafting SSS, the fiber of LFs was notably thicker, with increasingly smooth irregular surface. Based on surface morphological and colour change, the grafting of SSS on LFs was revealed upon irradiation of high-energy electron beams.

TGA was used to investigate the thermostability of the as-obtained samples (Schio et al., 2021; Chen et al., 2021). Fig. 3a displays TGA and DSC curves of LFs and LFs-PSSS. Notably, LFs-PSSS is thermally degraded in three stages. In stage 1 (T < 265 °C), LFs were degraded slightly compared with LFs-SSS. Which could be related to the weight loss at approximately 100 °C because of adsorbed water losses (Adewuyi and Pereira, 2017; Gupta et al., 2013). The original weight loss at T > 100 °C could possibly be attributed to water molecular loss,while the degree of degradation above 200 °C may be based on hemicellulose components and thermally unstable cellulose production. In stage 2, (265–480 °C), the organic components of LFs-PSSS decomposed to char and volatiles. LFs-PSSS exhibit a 51 % weight loss at 265–480 °C, while LFs exhibits a 62 % weight loss. In stage 3, (480 to 800 °C), cellulose and hemicellulose disintegrated into char. Therefore, LFs-PSSS revealed an increased thermostability following radiation grafting because SSS polymer chain with thermostability was introduced.

Fig. 3b displays the DSC curves of LFs and LFs-PSSS. Endothermic peaks were observed at 95 and 106 °C, respectively. The peak was slightly shifted after grafting with SSS, which was related to the glass transition that allows the mobility between amorphous polymers (Schio et al., 2021).

Fig. 4 displays the XPS spectra of LFs-PSSS before and after methylene blue adsorption. Notably, key elements were existed on LFs-PSSS before and after adsorption. According to Fig. 4a, XPS scanned spectra of LFs-PSSS displayed novel peaks of S 2p and Na 1 s signals, which resulted from the existence of sulphur and sodium atoms within their grafted SSS chain. These results further verified that SSS was successfully grafted onto the LFs surface. After adsorption, Na 1 s peaks disappeared, which attributed to the chloridion in MB was reacted with the sodion in LFs-PSSS.

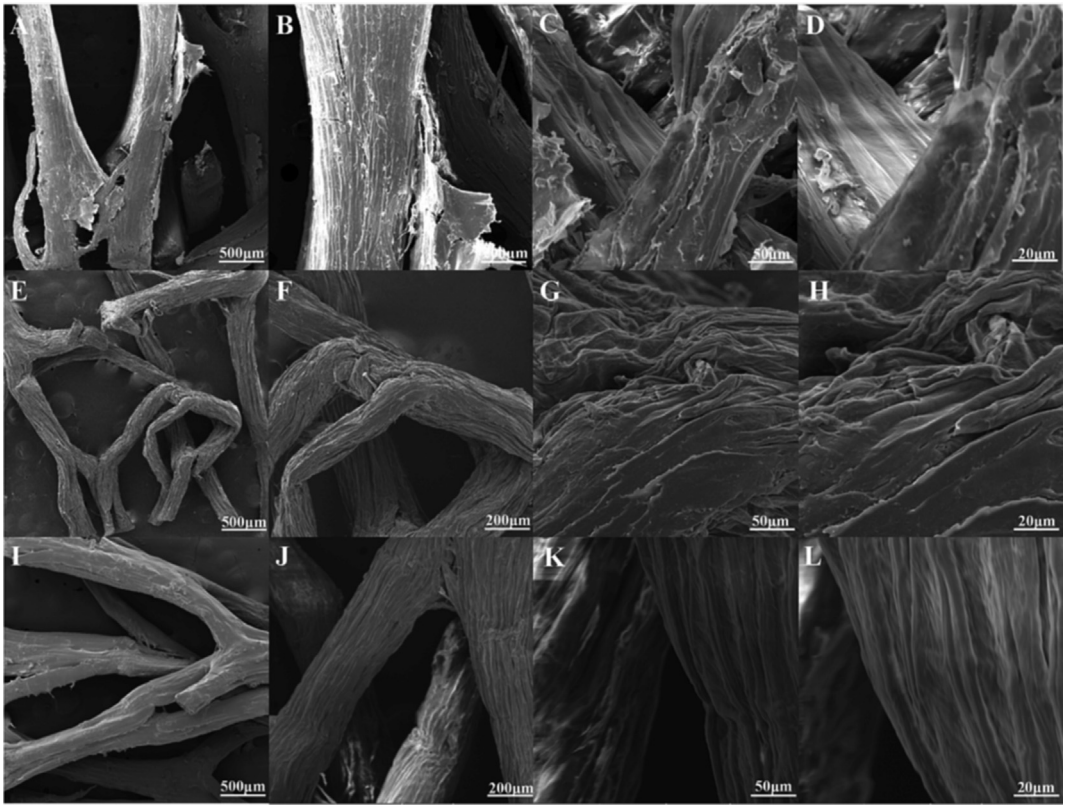

Fig. 2 SEM images of raw-LFs (A-D), LFs (E-H) and LFs-PSSS (I-L).

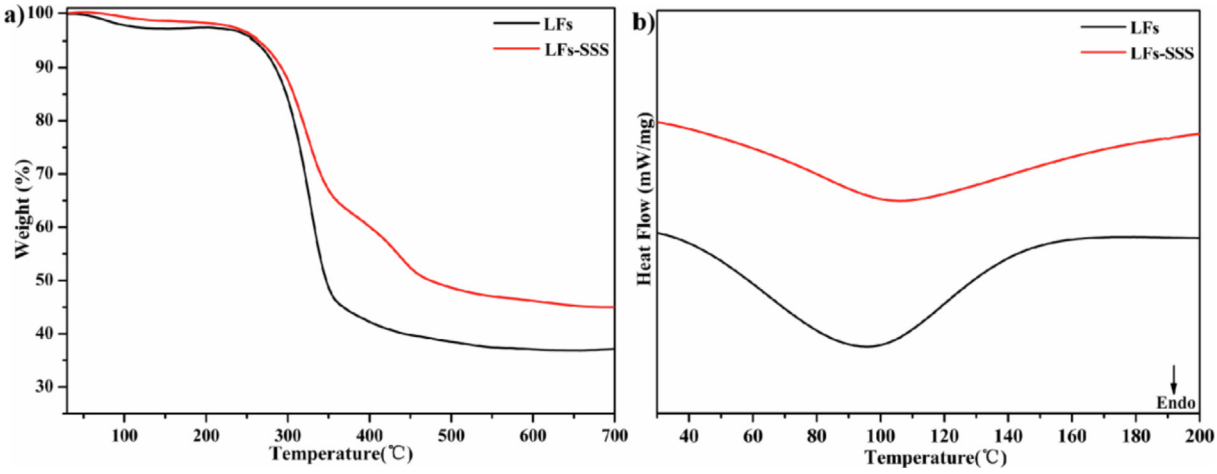

Fig. 3 TG curves (a) and DSC curves (b) of LFs and LFs-PSSS.

Generally speaking, when an atom is combined with more electron-conjugated groups, the binding energy of the inner electrons decrease due to the increase in the density of the outer electrons (Men et al., 2021). The C1s spectra of LFs-PSSS before and after MB adsorption (Fig. 4b) were shifted from 284.81, 286.47 and 287.68 eV to 284.73, 286.04 and 287.10 eV, indicated that the benzene ring in adsorbent receives electrons from the MB molecule, which validated π-π interaction is formed between them (Shi et al., 2020).

The N1s spectra were represented in Fig. 4c, the peaks at 399.98 and 401.61 eV removed to 399.55 and 401.87 eV, suggesting that N was participated in the MB adsorption through the electrostatic interaction between $= N^{+}(CH_3)_2$ and $-SO^{3-}$. Fig. 4d shows the O 1 s spectra, the peaks of O 1 s present at 532.44 and 533.29 eV shifted to 532.30 and 533.14 eV, the binding energy were quite similar, indicated that O atoms basically were not involved in the reaction. It can be clearly observed from the Fig. 5e that S2p were deconvoluted to

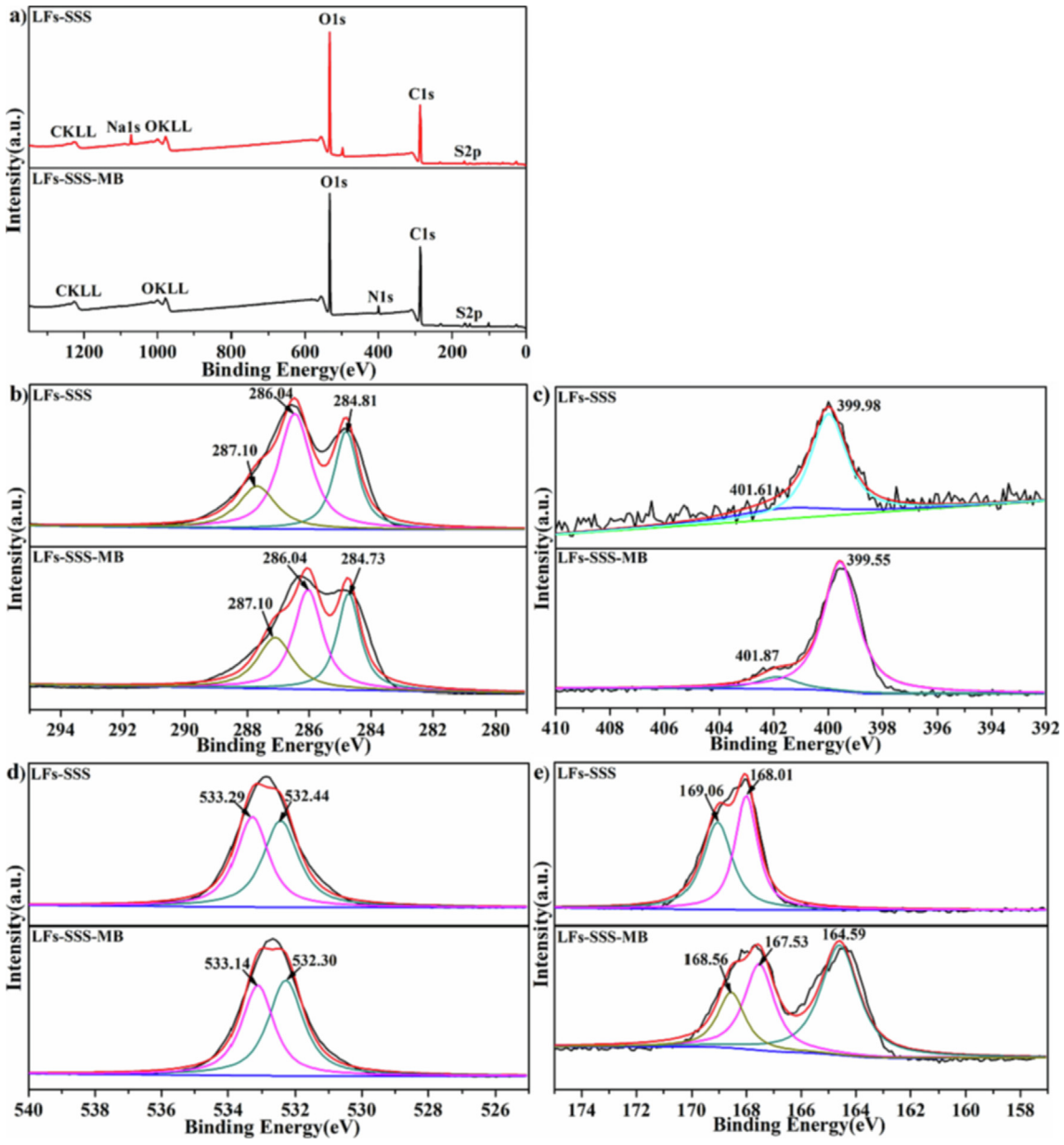

Fig. 4 XPS spectra of LFs-PSSS before and after MB uptake; Survey scans (a); high-resolution scans for C1s peaks (b); N1s peaks (c); O1s peaks(d); S2p peaks (e).

two significant bands at 168.01 and 169.06 eV, shifted to 167.53 and 168.56 eV, and a new peak at 164.59 eV appeared in the S2p spectrum after MB adsorption, indicated that the $-SO_3$ was introduced into the biosorbent after the MB adsorption.

3.2. Effect of SSS concentration

Sodium 4-vinylbenzene sulfonate (SSS) concentration were investigated for achieving the optimal adsorption efficiency. The effect of SSS concentration on GY was investigated at an absorbed dosage of 200 kGy (Fig. 5). The GY elevated to its maximum till the concentration of SSS at 20 wt%. Furthermore, the adsorption capacity exhibited an increasing trend as the SSS concentration increased (Chen et al., 2021). The result shows that, the concentration of SSS 20 wt%, grafting rate 40.45 %, and absorbed dosage 200 kGy were considered to be the best conditions for preparing LFs-PSSS.

3.3. Effect of absorbed dose

For attaining the highest adsorption efficiency, the absorbed dose was analyzed. Notably, the absorbed dose is a critical factor during grafting, which could intuitively determine the active radical center number and considerably affect grafting efficiency (Du et al., 2021).

The effects of grafting efficiency and adsorption capacity under the condition of radiation absorbed dose ranging from 20 to 240 kGy (dose rate 20 kGy/pass) were studied. Fig. 6 displays GY and adsorption capacity against the absorbed dose.

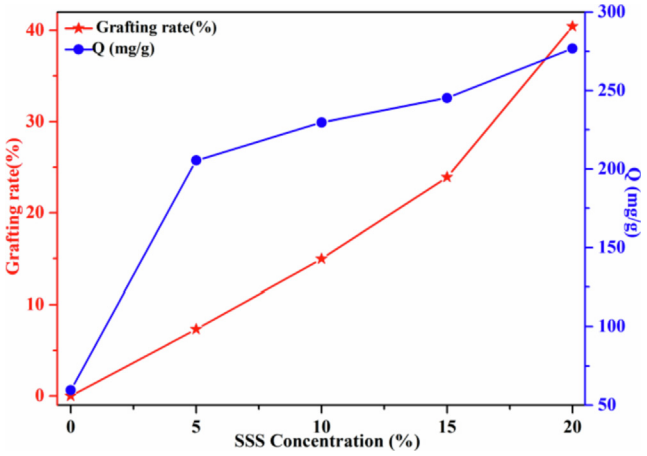

Fig. 5 The effect of the SSS concentration on the GY and adsorption capacity. (absorbed dosage = 200 kGy, Dose rate = 20 kGy/pass, contact time = 24 h, C_0 = 300 mg/L; pH = 7).

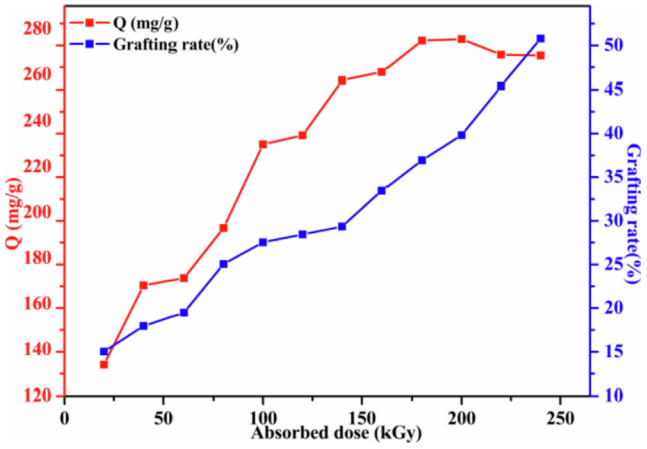

Fig. 6 Changes in the adsorption capacity and grafting rate depending on the absorbed dose (dose rate = 20 kGy/pass, SSS 20 wt%, contact time = 24 h; C_0 = 300 mg/L; pH = 7).

In the range of 20–200 kGy absorbed dosage, adsorption capacity increased, which subsequently decreased after the absorbed dosage exceeded 200 kGy. Typically, the maximal adsorption capacity (275.6 mg/g) was obtained at 200 kGy.

The increased absorbed dose indicates a higher number of free radicals, as well as more SSS monomers grafted onto LFs, it was able to increase the adsorption capacity. For co-irradiation grafting polymerization, the greater absorbed dosage could induce more homopolymer (PSSS) generation. Thus, when absorbed dosage > 200 kGy, the adsorption capacity decreased. Therefore, 200 kGy was chosen as the optimal radiation dose.

3.4. Effect of pH and zeta potential

The pH considerably affects the absorbent's ionization degree, surface charge, active sites and adsorbent structure. Thus, the effect of pH on uptake capacity was investigated. Fig. 7a displayed the adsorption capacity of LFs-PSSS for MB and its zeta potential at pH 2.0 to 12.0 at 298.15 K. Notably, a rapid increase appeared in MB uptake with the increase of the MB solution pH. For LFs-PSSS, when the pH was 7, its adsorption capacity reached 275.26 mg/g. Furthermore, adsorption capacity revealed no significant increase when the pH increased continuously. Therefore, in this study, pH = 7 was used in subsequent experiments. However, LFs exhibited lower adsorption capacity throughout the whole pH range, especially when the pH < 3.

For the purpose of further investigating the adsorption mechanism, the zeta potential was measured to examine the surface charges of LFs and LFs-PSSS at pH 2.0–12.0, respectively. Fig. 7b displayed the zeta potential curves for LFs and LFs-PSSS. LFs was exhibited a pHzpc (pH at zero-point charge) of 3.0. For LFs, the positive surface potential can be associated with hydroxyl protonation based on hemicellulose and cellulose. After the introduction of polyanionic electrolyte SSS onto LFs, the zeta potential of LFs-PSSS was much lower than that of LFs in the entire pH range, which indicated the successful grafting of SSS (Shi et al., 2020). As pH elevates, zeta potentials become negative and decrease, resulting in LFs-PSSS exhibiting high density of negative charges. The increase in pH was beneficial to deprotonation. Thus, the adsorption of electrostatic interaction-based cation dyes was facilitated. This phenomenon is consistent with XPS results.

3.5. Dosage of LFs-PSSS

The effect of adsorbent dosage was also investigated in this research. Notably, LFs-PSSS achieved a high adsorption efficiency, especially at the lower concentration. According to Fig. 8, when the LFs-PSSS concentration increased within 0.5–2.5 g/L, MB removal efficiency gradually increased from 43.58 % to 93.31 %. However, the adsorption capacity gradually decreased from 439.41 to 188.16 mg/g because with the increase in the dosage of adsorbent, the number of active sites in the adsorbent increased, which enhanced removal efficiency. However, excessive active sites of the adsorbent were observed at high dosage, which lead to a decrease in the adsorption capacity for each adsorbent (Chen et al., 2021). Considering both the adsorption capacity and removal efficiency, the 1.0 g/L LFs-PSSS was considered to be the optimal dosage for adsorbing MB.

3.6. Initial concentration and adsorption isotherm

The effect of initial concentration was investigated in this study. According to Fig. 9a, as the initial concentration of MB increased, the adsorption capacity increased rapidly at first, and subsequently increased slowly. Finally, the adsorption equilibrium was achieved. The higher the temperature is, the more obvious this trend is. An adsorption capacity of 409.67 mg/g can be achieved at 318.15 K.

To investigate the relationship of the initial concentration of MB solution with adsorption capacity at various temperatures, the adsorption isotherms were studied. Adsorption isotherms were conducted at three temperatures (298.15, 308.15, 318.15 K) with diverse initial MB concentrations (50–600 mg·L^{-1}). The mixed sample was shaken for 24 h to ensure equilibrium adsorption. Langmuir (Zhang et al., 2022) and

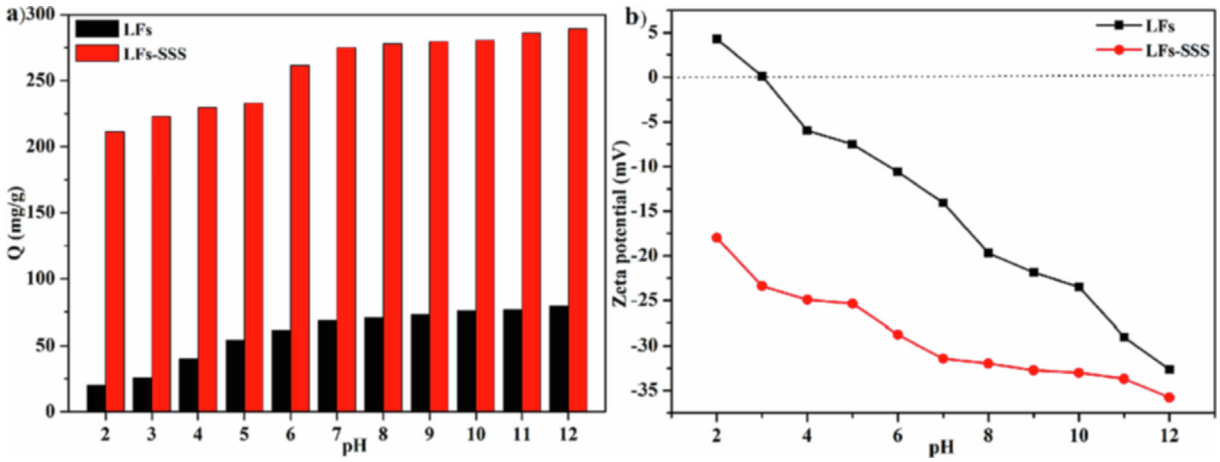

Fig. 7 (a) Effect of initial pH on the MB adsorption of LFs and LFs-PSSS; (b) The pH dependence of Zeta potential for LFs and LFs-PSSS (Dose rate = 20 kGy/pass, SSS 20 wt%, C_0 = 300 mg/L; contact time = 24 h).

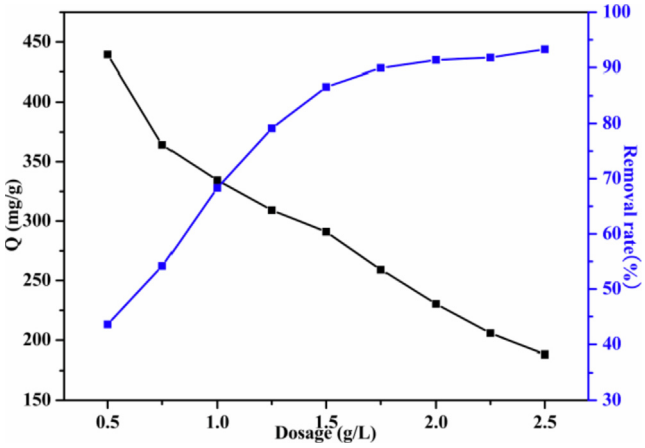

Fig. 8 Effect of LFs-PSSS dosage on adsorption capacity and removal rate (dose rate = 20 kGy/pass, SSS 20 wt%, contact time = 24 h; C_0 = 500 mg/L; pH = 7).

Freundlich models (Li et al., 2021) were used to investigate adsorption isotherms, as follows:

$$Q_e = \frac{Q_m K_L C_e}{1 + K_L C_e} \tag{5}$$

$$Q_e = K_F C_e^{1/n} \tag{6}$$

where Q_e (mg·g^{-1}) and C_e (mg·L^{-1}) represent adsorption capacity and MB concentration under equilibrium respectively; K_L (L/mg) is the Langmuir constant, Q_m (mg/g) is maximal MB adsorption; $1/n$ represents the heterogeneity factor, and K_F (mg$^{1-1/n}$·L$^{1/n}$·g^{-1}) denotes the Freundlich constant (indicating adsorption level).

The isotherm curves of MB onto LFs-PSSS were displayed in Fig. 9b. Langmuir and Freundlich were used to fit the adsorption isotherm (Fig. 9c-d). Table 1 displays the obtained adsorption isotherm parameters. Langmuir exhibited an increased linear correlation ($R^2 > 0.99$) compared with Freundlich ($R^2 < 0.86$). Thus, a higher fitting degree of the Langmuir model revealed that MB adsorption onto LFs-PSSS was close to a monolayer process. Similar findings were reported for various adsorbent-methylene blue systems in literature (Duman et al., 2016; Duman et al., 2020). At 318.15 K, the calculated maximum adsorption capacity was 416.67 mg/g, which is very close to the experimental result of 409.67 mg/g.

3.7. Contact time and adsorption kinetics

As shown in Fig. 10(a), when at the low initial concentration of MB, the adsorption was reached equilibrium quickly. With the increase of the MB initial concentration, the time for adsorption to reach equilibrium is prolonged. This phenomenon was more obvious with the higher of the initial concentration of MB. This might be attributed to the following reasons. Firstly, when the surface adsorption sites of the LFs-PSSS were occupied, MB molecules take longer to reach the interior sites; Next, as the adsorption capacity increased, electrostatic repulsion occurs between the MB being adsorbed and unabsorbed, leading to the adsorption resistance of MB.

For further exploring the adsorption behavior and rate-control steps, three kinetic adsorption models were investigated(Fig. 10 c-d). Samples were obtained at specific intervals and tested for remaining MB concentration. The adsorption kinetics of MB onto LFs-PSSS were analyzed with pseudo-first-order (Khadir et al., 2020a), pseudo-second-order (Franco et al., 2021), and particle diffusion (Shi et al., 2020) models, respectively. The three Kinetic models were presented in Table S2.

Obviously, as showed in Table 2, the R^2 obtained from the pseudo-second-order model was larger than that from the pseudo-first-order model. Based on the aforementioned findings, chemisorption was controlled MB adsorption onto LFs-PSSS. This result is consistent with literature (Ayranci et al., 2009; Duman et al., 2020).

In this study, the intra-particle diffusion model was applied to analyse the kinetics as well as the diffusion mechanism for adsorption. Fig. 10(d) reveals that adsorption was affected by three stages. Table S3 displays data extracted based on linear fit plots for the model. The values of C_1, C_2, and $C_3 \neq 0$, indicating that no single intra-particle diffusion was observed among the three stages. The three-stage diffusion was corresponded to outer membrane or boundary layer diffusion, pore

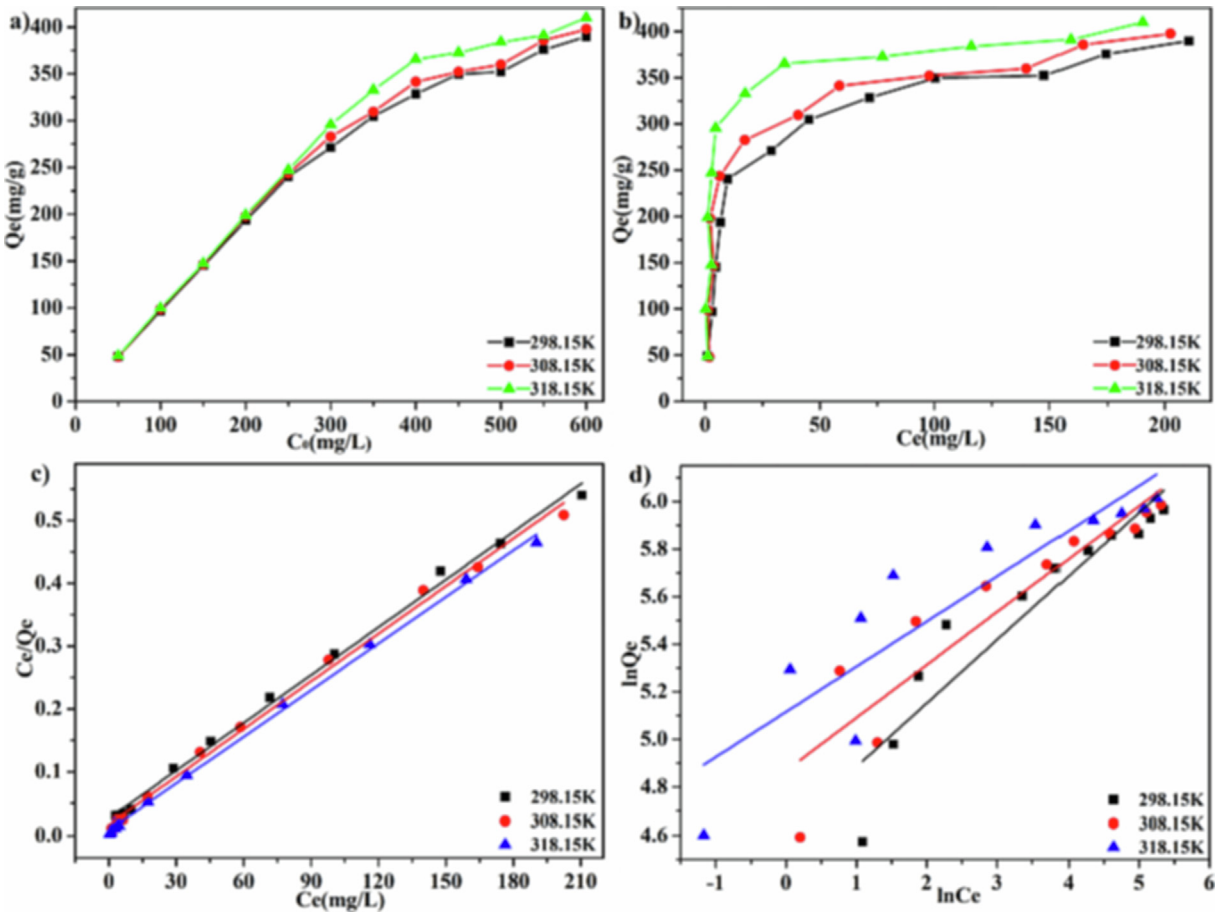

Fig. 9 The effect of initial concentration in LFs-PSSS adsorption (a); The isotherm curves of MB onto LFs-PSSS (b); linearised Langmuir (c) as well as Freundlich (d) isotherm model with different temperature.

Table 1 Isothermal parameters of MB onto LFs-PSSS.

Adsorption isotherm model	Parameters	Temperature (K)		
		298.15	308.15	318.15
Langmuir	Q_m(mg/g)	395.23	395.26	416.67
	K_L(L/mg)	0.0966	0.1501	0.3200
	R^2	0.9962	0.9956	0.9983
Freundlich	K_F($mg^{1-1/n}\cdot L^{1/n}\cdot g^{-1}$)	101.27	130.13	166.62
	n	3.7438	4.4946	5.2612
	R^2	0.8670	0.8434	0.7988

diffusion, and adsorption–desorption equilibrium, respectively (Li et al., 2020). As presented in Table S3, the first stage described the boundary layer diffusion of MB, it was a fast transient adsorption. Stage 2 involved gradual adsorption, and MB molecules diffuse within the particle through the grafted PSSS. The intra-particle diffusion process reached the equilibrium stage because of the decreased MB concentration in solution as well as the reduced number of adsorption active sites.

3.8. Adsorption thermodynamics

The effect of temperature on the adsorption were investigated. The thermodynamic parameters and values of MB onto LFs-PSSS at various temperature and concentration were presented in Table 3. Based on the results, an increased temperature led to a higher adsorption capacity, which indicated that MB adsorption by the adsorbent belonged to an endothermic reaction. The determined entropy change ΔS ($J\cdot mol^{-1}\ K^{-1}$),

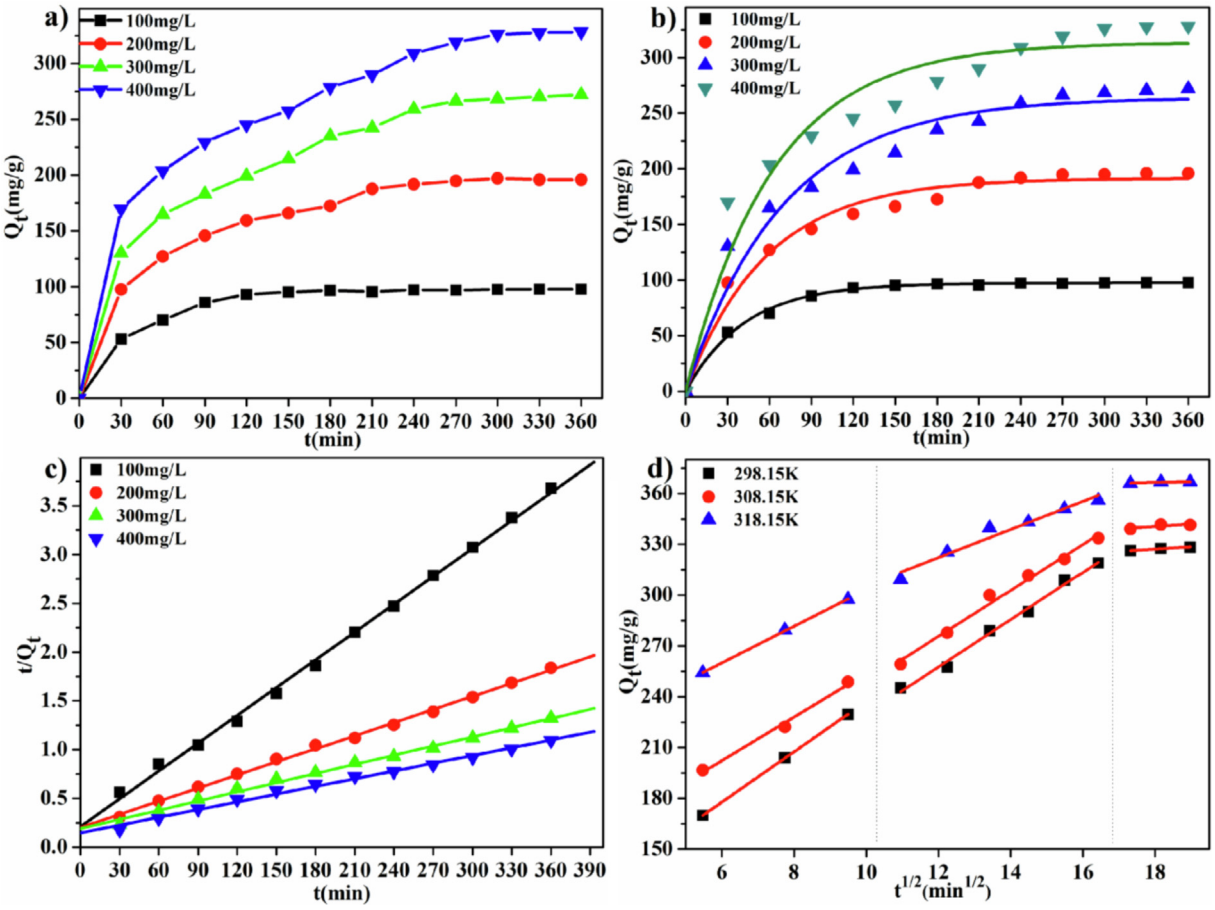

Fig. 10 (a) Curves displaying MB adsorption dynamics on LFs-PSSS; (pH = 7, T = 298.15 K) Simulated plots of pseudo-first-order; (b) and pseudo-second-order (c) models;(d) MB intra-particle diffusion model onto LFs-PSSS.(pH = 7, C_0 = 400 mg/L).

Table 2 Kinetic parameters of two models regarding MB adsorption at 298.15 K.

Adsorption kinetics models	Parameters	Initial dye concentration (mg/L)			
		100	200	300	400
Pseudo-first-order	$q_{e,exp}$(mg/g)	97.92	195.88	271.91	328.32
	$q_{e,cal}$(mg/g)	97.45	191.50	264.00	313.61
	k_1(min^{-1})	0.0239	0.0175	0.0145	0.0161
	R^2	0.9964	0.9755	0.9576	0.9426
Pseudo-second-order	$q_{e,exp}$(mg/g)	97.92	195.88	271.91	328.32
	$q_{e,cal}$(mg/g)	105.15	223.21	318.47	378.79
	k_2($\times 10^{-3}$) (g·mg^{-1}·min^{-1})	0.4305	0.0995	0.0521	0.0474
	R^2	0.9979	0.9978	0.9939	0.9928

enthalpy change ΔH (kJ·mol^{-1}), and Gibbs free energy change ΔG (kJ·mol^{-1}) according to the following equations (Hong et al., 2019):

$$\ln\left(\frac{Qe}{Ce}\right) = -\frac{\Delta H}{RT} \times \frac{1}{T} + \frac{\Delta S}{R} \tag{10}$$

$$\Delta G = \Delta H - T\Delta S \tag{11}$$

Table 3 displayed the calculated values for thermodynamic parameters, ΔG had a negative value, which implied the spontaneous and thermodynamically favourable process of MB adsorption onto LFs-PSSS. Furthermore, ΔG value decreased as the temperature increased, which indicated that an increase in temperature is conducive to the spontaneous progress of the adsorption reaction.

Table 3 Calculated adsorption thermodynamic data of MB onto LFs-PSSS.

Concentration (mg/L)	T(K)	$\ln(Q_e/C_e)$	Thermodynamic parameter			
			ΔH (kJ·moL^{-1})	ΔS (J·moL^{-1}·K^{-1})	ΔG (kJ·moL^{-1})	R^2
200	298.15	3.38	73.21	274.17	−8.38	0.9865
	308.15	4.53			−11.60	
	318.15	5.23			−13.85	
300	298.15	2.24	75.42	295.38	−5.56	0.9346
	308.15	2.80			−7.17	
	318.15	4.17			−11.02	
400	298.15	1.52	32.80	122.16	−3.77	0.9350
	308.15	1.76			−4.52	
	318.15	2.36			−6.24	
	308.15	0.68			−1.73	
	318.15	2.15			−5.69	

The positive ΔS indicated that the adsorption is random on the surface of LFs-PSSS. Furthermore, MB adsorption increased the freedom degree of the entire system. Here, ΔH exhibited a positive value, thus, the endothermic adsorption process was achieved only at a high temperature. This result was associated with the increased active sites at a high temperature (Li et al., 2020).

3.9. Adsorption mechanism

The possible mechanism of MB uptake is illustrated in Fig. 11 According to the result of experiment, MB adsorption can be assigned to a monolayer chemisorption process. Furthermore, pH, zeta potentials, FT-IR and XPS analysis were revealed that the electrostatic interaction was involved in the process of adsorption. Besides, the aromatic rings with conjugated double bonds could lead to the possibility of π-π stacking (Fu et al., 2020). According to the FT-IR spectra of LFs-PSSS/MB (Fig. S2), we can clearly see that the peaks at 1334 and 1056 cm^{-1} was assigned to C—S stretching of MB, which implies MB has been successfully adsorbed on the surface of the LFs-PSSS. The band at 1636 cm^{-1} of LFs-PSSS was attributed to the typical benzene ring skeleton vibration absorption. However, it was moved to 1601 cm^{-1} after MB adsorption, which could be due to the π-π stacking formed between the LFs-PSSS and MB, and the results were consistent with the characterization of XPS. The hydrogen bonds interaction also plays a part role in promoting the adsorption of MB by LFs-PSSS. Altogether, the hydrogen bonding, electrostatic interaction, and π-π stacking interaction are proposed as the possible mechanism for MB uptake.

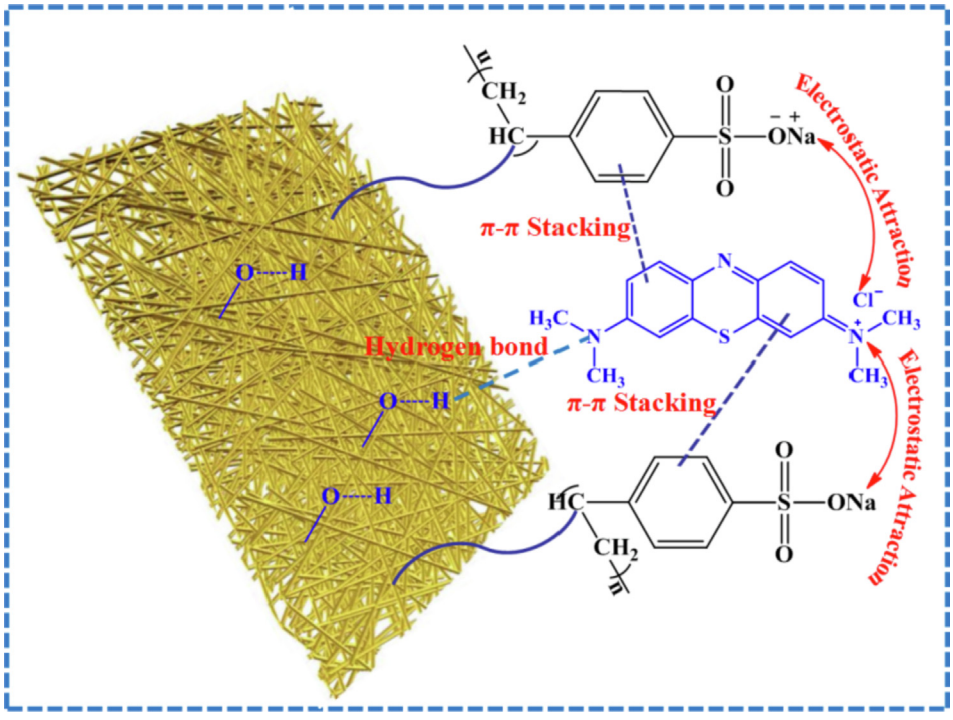

Fig. 11 Possible adsorption mechanism of MB onto LFs-PSSS.

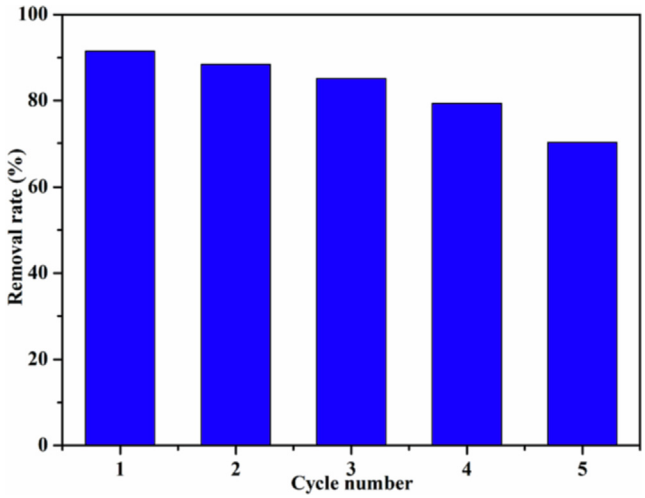

Fig. 12 Adsorption-desorption cycles of LFs-PSSS.

The atomic percentage beofore and after MB capture by XPS was showed in Table S4, Element content of N revealed that the original adsorbent contains almost no N element. After MB adsorption, the content of N element increases from 0.04 % to 3.22 %, which is mainly caused by the N in MB molecule, indicating that MB has been successfully adsorbed by LFs-PSSS.

3.10. Other dyes adsorption

To investigate the adsorption selectivity of LFs-PSSS, other dyes such as, Congo red, methyl orange, and rhodamine B were adsorbed for comparison. According to Fig.S3, LFs-PSSS exhibited favourable adsorption performance for cationic dyes. However, no adsorption was observed on anionic dyes. Moreover, its adsorption for Congo red, methyl orange and rhodamine B reached 11.59, 9.85 and 86.34 mg/g, respectively, at 298.15 K.

3.11. Desorption and regeneration

Reusability is one of the key indicators to evaluate whether an adsorbent is suitable for practical application. Experiments revealed that the LFs-PSSS blocks adsorbent could be easily separated from solutions by physical means through a tweezers. The desorption of MB from LFs-PSSS was conducted by immersing the LFs-PSSS-MB in 10 % NaCl solution under continuous stirring for 3 h at room temperature. Fig. 12 shows the removal rate of MB with the increasing cycle times, due to the adsorbent loss during recycles. Notably, the removal rate were all over 85 % after three-time recycles, what's more, the removal rate could still > 70 % after five cycles. The results provided sufficient evidences that the biomass derivatives of LFs-PSSS prepared in this study has outstanding reusability.

3.12. Comparison of loofah-based adsorbents of MB adsorption

For verifying enhancement of LFs-PSSS adsorption performance following radiation modification, the uptake capacity of LFs and LFs-PSSS were investigated in this study. 20 mg LFs and LFs-PSSS were added into 20 mL of MB solution with different concentration (pH = 7.0, T = 298.15 K) in a clear glass bottle. Then, the mixed sample was transferred into the thermostat shaker, shaked for 24 h, followed by filtering and measurement of eventual MB concentration. According to Fig. 13a, LFs-PSSS exhibited a threefold adsorption capacity compared with LFs, which indicated that LFs-PSSS exhibited high adsorption performance for MB. Fig. 13b displays the UV–vis absorption spectra of MB solution after absorption by LFs and LFs-PSSS. The MB solution absorbance declined substantially, which indicated that MB molecules were mostly eliminated by LFs-PSSS. According to the colour image of the dye solution, the MB could be efficiently removed by LFs-PSSS.

Table 5 compares MB removal efficiency from the perspectives of maximal adsorption capacity (Q_{max}) of LFs-PSSS for

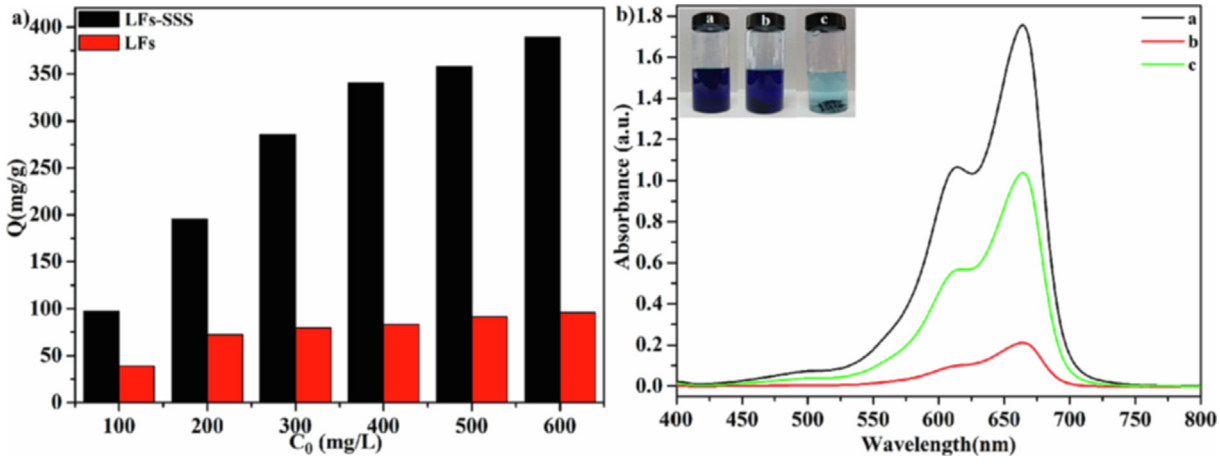

Fig. 13 a) The adsorption capacity of LFs and LFs-PSSS under diverse concentration; b) UV–vis absorption spectra of MB solution after LFs and LFs-PSSS absorption, inset picture reveals the MB solution of the original MB solution (a) with LFs(b) and with LFs-SSS (c) diluted to 10 mg/L.

Table 5 Comparison of LFs-PSSS and other loofah-based adsorbents over MB.

Loofah based adsorbents	contact time	pH	Temperature	Q_{max} of MB (mg/g)	Reference
LFs-PSSS	360 min	7.0	318.15 K	409.67	This work
Cellulose isolated from Luffa cylindrica	120 min	7.3	298.15 K	36.20	Oun et al., 2021
loofah-based porous carbons	120 min	–	288.15 K	210.97	Li et al., 2017
LF-g-PAA composite	25 h	7.3	298.15 K	180.20	Liang et al., 2020
Reduced graphene oxide modified luffa sponge	250 min	7.0	298.15 K	63.32	Li et al., 2015
Biomass fiber -Luffa cylindrica	20 min	5.8	293.15 K	49.46	Boudechiche et al., 2016
Luffa cylindrica fibers	120 h	–	293.15 K	49.00	Demir et al., 2008
Acrylic acid grafted cellulosic Luffa cylindrical fiber	250 min	7.0	318.15 K	62.15	Gupta et al., 2013
Luffa peels	240 min	4.0–10.0	308.15 K	124.00	Mallampati et al., 2015

MB with other loofah based adsorbents in literature. Due to the loofah based adsorbents modified with different monomer revealed distinct structural characteristics, such as chemical composition, specific surface area and functional groups, their adsorption performance also exhibited considerable difference. Overall, LFs-PSSS outperformed the majority of other loofah-based adsorbents. The superb adsorption performance of LFs-PSSS could effectively absorbed MB, because the grafted PSSS was a polyanion electrolyte, that makes the adsorbent take a large number of negative charges, so cationic dyes could be adsorbed through electrostatic interaction.

4. Conclusions

In this study, an anionic functionalised LFs-PSSS was prepared by grafting SSS onto LFs fibers through electron beam radiation. The obtained LFs-PSSS exhibited potent MB adsorption capacity, and its adsorption capacity reached 409.67 mg/g at 318.15 K, which was superior to most of other luffa-based adsorbents. The adsorption process was pH controlled, and the optimal pH was 7.0. According to the adsorption experimental results, MB adsorption can be accurately described by using Langmuir isotherm and pseudo-second-order kinetic models. Typically, π-π interaction and hydrogen bonds interaction plays a vital role in promoting the adsorption of MB, associated with the electrostatic interaction of $-SO_3^-$ with $=N^+(CH_3)_2$. According to thermodynamic parameters, MB adsorption was an entropy-driven endothermic process. In addition, the biosorbent exhibited excellent reusability. Altogether, electron-beam-radiation-based modification can efficiently enhanced the adsorption ability of LFs, LFs-PSSS might serve as an eco-friendly adsorbent in dye-containing wastewater treatments.

CRediT authorship contribution statement

Yuan Zhao: Investigation, Writing – original draft, Writing – review & editing. **Tao Chen:** Conceptualization, Investigation. **Xiao-Fang Song:** Supervision. **Jin-Yu Yang:** Supervision. **Ya-Yang Wang:** Supervision. **Yue-Sheng Li:** Project administration. **Yi Liu:** Writing – review & editing, Project administration.

Declaration of Competing Interest

The authors declare that they have no known competing financial interests or personal relationships that could have appeared to influence the work reported in this paper.

Acknowledgment

This work was supported by grants from the National Natural Science Foundation of China, China (No.51903080), Foundation of Hubei Provincial Department of Education, China (No.T2020022, D20212801).

Appendix A. Supplementary material

Supplementary data to this article can be found online at https://doi.org/10.1016/j.arabjc.2022.104382.

References

Adewuyi, A., Pereira, F.V., 2017. Underutilized Luffa cylindrica sponge: a local bio-adsorbent for the removal of Pb (II) pollutant from water system. Beni-Suef. U. J. Basic. 6, 118–126. https://doi.org/10.1016/j.bjbas.2017.02.001.

Akter, t., Bañuelos, J.L., Andrade, D., Bañuelos, D.I., Saupe, G.B., 2022. Rapid Adsorption Mechanism of Methylene Blue onto a Porous Mixed Ti-Nb Oxide. Mater. Chem. Horizons, 1(1), 49-67. DOI: 10.22128/MCH.2022.555.1006.

Aldahash, S.A., Higgins, P., Siddiqui, S., Uddin, M.K., 2022. Fabrication of polyamide-12/cement nanocomposite and its testing for different dyes removal from aqueous solution: characterization, adsorption, and regeneration studies. Sci. Rep. 12, 13144. https://doi.org/10.1038/s41598-022-16977-8.

Alizadeh, E., Baseri, H., 2022. Photocatalytic degradation of sumatriptan succinate by ZnO, Fe doped ZnO and TiO_2-ZnO nanocatalysts. Mater. Chem. Horiz. 1, 7–21. https://doi.org/10.22128/MCH.2022.534.1002.

Alvarado-Gómez, E., Tapia, J.I., Encinas, A., 2021. A sustainable hydrophobic luffa sponge for efficient removal of oils from water. Sustain. Mater. Techno. 28, e00273.

Anastopoulos, I., Pashalidis, I., 2019. The application of oxidized carbon derived from Luffa cylindrica for caffeine removal. equilibrium, thermodynamic, kinetic and mechanistic analysis. J. Mol. Liq. 296,. https://doi.org/10.1016/j.molliq.2019.112078 112078.

Anastopoulos, I., Pashalidis, I., 2020. Environmental applications of Luffa cylindrica-based adsorbents. J. Mol. Liq. 319,. https://doi.org/10.1016/j.molliq.2020.114127 114127.

Ayranci, E., Duman, O., 2009. In-situ UV-visible spectroscopic study on the adsorption of some dyes onto activated carbon cloth. Sep. Sci. Technol. 44, 3735–3752. https://doi.org/10.1080/01496390903182891.

Babaei, M., Ghaee, A., Nourmohammadi, J., 2019. Poly (sodium 4-styrene sulfonate)-modified hydroxyapatite nanoparticles in zein-

based scaffold as a drug carrier for vancomycin. Mat. Sci. Eng. C-Mater. 100, 874–885. https://doi.org/10.1016/j.msec.2019.03.055.

Boudechiche, N., Mokaddem, H., Sadaoui, Z., Trari, M., 2016. Biosorption of cationic dye from aqueous solutions onto lignocellulosic biomass (Luffa cylindrica): characterization, equilibrium, kinetic and thermodynamic studies. J. Ind. Eng. Chem. 7, 167–180. https://doi.org/10.1007/s40090-015-0066-4.

Chen, T., Zhao, Y., Sang, Y.N., Tang, M., Hu, G.W., Han, X.B., Gao, J., Ma, R., 2021. Facile synthesis of magnetic CS-g-SPSS microspheres via electron beam radiation for efficient removal of methylene blue. J. Saudi. Chem. Soc. 25,. https://doi.org/10.1016/j.jscs.2021.101299 101299.

Demir, H., Top, A., Balköse, D., Ülkü, S., 2008. Dye adsorption behavior of Luffa cylindrica fibers. J. Hazard. Mater. 153, 389–394. https://doi.org/10.1016/j.jhazmat.2007.08.070.

Du, J.F., Dong, Z., Yang, X., Zhao, L., 2020. Radiation grafting of dimethylaminoethyl methacrylate on cotton linter and subsequent quaternization as new eco-friendly adsorbent for phosphate removal. Environ. Sci. Pollut. R. 27, 24558–24567. https://doi.org/10.1007/s11356-020-08712-5.

Du, W.J., Fan, J.X., Ma, R., Yang, G., Liu, J.Q., Zhang, S.F., Chen, T., 2021. Radiation-initiated chitosan-based double network hydrogel: synthesis, characterization, and adsorption of methylene blue. J. Appl. Polym. Sci. 138, 51531. https://doi.org/10.1002/app.51531.

Duman, O., Tunç, S., Polat, T.G., 2015. Adsorptive removal of triarylmethane dye (Basic Red 9) from aqueous solution by sepiolite as effective and low-cost adsorbent. Micropor. Mesopor. Mat. 210, 176–184. https://doi.org/10.1016/j.micromeso.2015.02.040.

Duman, O., Tunç, S., Polat, T.G., Bozoğlan, B.K., 2016. Synthesis of magnetic oxidized multiwalled carbon nanotube-κ-carrageenan-Fe3O4 nanocomposite adsorbent and its application in cationic Methylene Blue dye adsorption. Carbohyd. Polym. 147, 79–88. https://doi.org/10.1016/j.carbpol.2016.03.099.

Duman, O., Polat, T.G., Diker, C.Ö., Tunç, S., 2020. Agar/κ-carrageenan composite hydrogel adsorbent for the removal of Methylene Blue from water. Int. J. Biol. Macromol. 160, 823–835. https://doi.org/10.1016/j.ijbiomac.2020.05.191.

Feng, X.A., Cheng, Y.X., Zhou, P.C., Chen, S.X., Wang, X.J., He, P., Nie, X.Q., Dong, F.Q., 2021. Fabrication of novel carboxyl and amidoxime groups modified luffa fiber for highly efficient removal of uranium(VI) from uranium mine water. J. Environ. Chem. Eng. 9,. https://doi.org/10.1016/j.jece.2021.105681 105681.

Franco, D.S.P., Georgin, J., Netto, M.S., Allasia, D., Oliverira, M., Foletto, E.L., Dotto, G.L., 2021. Highly effective adsorption of synthetic phenol effluent by a novel activated carbon prepared from fruit wastes of the Ceiba speciosa forest species. J. Environ. Chem. Eng. 9,. https://doi.org/10.1016/j.jece.2021.105927 105927.

Fu, Q.M., Tan, X.F., Ye, S.J., Ma, L.L., Gu, Y.L., Zhang, P., Chen, Q., Yang, Y.Y., Tang, Y.Q., 2020. Mechanism analysis of heavy metal lead captured by natural-aged microplastics. Chemosphere 270,. https://doi.org/10.1016/j.chemosphere.2020.128624 128624.

Gao, B.J., Chen, T., Cui, K., 2017. Constituting of a new surface-initiating system on polymeric microspheres and preparation of basic protein surface-imprinted material in aqueous solution. Polym. Advan. Technol. 29, 575–586. https://doi.org/10.1002/pat.4167.

Gautam, S., Agrawal, H., Thakur, M., Akbari, A., Sharda, H., Kaur, R., Amini, M., 2020. Metal oxides and metal organic frameworks for the photocatalytic degradation: a review. J. Environ. Chem. Eng. 8,. https://doi.org/10.1016/j.jece.2020.103726 103726.

Gedam, A.H., Dongre, R.S., 2016. Activated carbon from Luffa cylindrica doped chitosan for mitigation of lead(ii) from an aqueous solution. RSC Adv. 27, 22639–22652. https://doi.org/10.1039/c5ra22580a.

Gupta, V.K., Agarwal, S., Singh, P., Pathania, D., 2013. Acrylic acid grafted cellulosic Luffa cylindrical fiber for the removal of dye and metal ions. Carbohyd. Polym. 98, 1214–1221. https://doi.org/10.1016/j.carbpol.2013.07.019.

Han, X.B., Li, R., Miao, P.P., Gao, J., Hu, G.W., Zhao, Y., Chen, T., 2022. Design, synthesis and adsorption evaluation of bio-based lignin/chitosan beads for Congo Red removal. Materials 15, 2310. https://doi.org/10.3390/ma15062310.

Hassanzadeh-Afruz, F., Heidari, G., Maleki, A., 2022. Magnetic nanocomposite hydrogel based on arabic gum for remediation of lead(II) from contaminated water. Mater. Chem. Horiz. 1, 107–122. https://doi.org/10.22128/MCH.2022.570.1013.

Hong, T.T., Okabe, H., Hidaka, Y., Omondi, B.A., Hara, K., 2019. Radiation induced modified CMC-based hydrogel with enhanced reusability for heavy metal ions adsorption. Polymer 181,. https://doi.org/10.1016/j.polymer.2019.121772 121772.

Khadir, A., Motamedi, M., Pakzad, E., Sillanpää, M., Mahajan, S., 2020a. The prospective utilization of Luffa fibres as a lignocellulosic bio-material for environmental remediation of aqueous media: a review. J. Environ. Chem. Eng. 9,. https://doi.org/10.1016/j.jece.2020.104691 104691.

Khadir, A., Negarestani, M., Mollahosseini, A., 2020b. Sequestration of a non-steroidal anti-inflammatory drug from aquatic media by lignocellulosic material (Luffa cylindrica) reinforced with polypyrrole: study of parameters, kinetics, and equilibrium. J. Environ. Chem. Eng. 8,. https://doi.org/10.1016/j.jece.2020.103734 103734.

Li, B., Guo, J.Z., Liu, J.L., Fang, L., Lv, J.Q., Lv, K.L., 2020. Removal of aqueous-phase lead ions by dithiocarbamate-modified hydrochar. Sci. Total. Environ. 714,. https://doi.org/10.1016/j.scitotenv.2020.136897 136897.

Li, Z.Q., Jiang, L.Y., Tang, C.J., 2019. Investigation on removing recalcitrant toxic organic polluters in coking wastewater by forward osmosis. Chinese. J. Chem. Eng. 28, 122–135. https://doi.org/10.1016/j.cjche.2019.07.011.

Li, S.F., Tao, M., Xie, Y.D., 2015. Reduced graphene oxide modified luffa sponge as a biocomposite adsorbent for effective removal of cationic dyes from aqueous solution. Desalin. Water. Treat. 57, 1106344. https://doi.org/10.1080/19443994.2015.1106344.

Li, S.Y., Teng, H.J., Guo, J.Z., Wang, Y.X., Li, B., 2021. Enhanced removal of Cr(VI) by nitrogen-doped hydrochar prepared from bamboo and ammonium chloride. Bioresource. Technol. 342,. https://doi.org/10.1016/j.biortech.2021.126028 126028.

Li, Z.C., Wang, G.Q., Zhai, K.L., He, C.C., Li, Q., Guo, P.Z., 2017. Methylene blue adsorption from aqueous solution by loofah sponge-based porous carbons. Colloid. Surface. A 538, 28–35. https://doi.org/10.1016/j.colsurfa.2017.10.046.

Li, Y.M., Zhang, Y., Zhang, Y., Wang, G.X., Li, S.Y., Han, R.M., Wei, W., 2018. Reed biochar supported hydroxyapatite nanocomposite: characterization and reactivity for methylene blue removal from aqueous media. J. Mol. Liq. 263, 53–63. https://doi.org/10.1016/j.molliq.2018.04.132.

Liang, C., Liu, Y., Yan, C.J., Zhou, S., 2020. Green synthesis of loofah fiber-based adsorbents with high adsorption performance for methylene blue. Mater. Lett. 284,. https://doi.org/10.1016/j.matlet.2020.128929 128929.

Liatsou, I., Constantinou, P., Pashalidis, I., 2017. Copper binding by activated biochar fibres derived from Luffa cylindrica. Water. Air. Soil. Poll. 228, 255. https://doi.org/10.1007/s11270-017-3411-8.

Mallampati, R., Tan, K.S., Valiyaveettil, S., 2015. Utilization of corn fibers and luffa peels for extraction of pollutants from water. Int. Biodeter. Biodegr. 103, 8–15. https://doi.org/10.1016/j.ibiod.2015.03.027.

Mehdizadeh, A., Moghadam, P.N., Ehsanimehr, S., Fareghi, A.R., 2022. Preparation of a new magnetic nanocomposite for the removal of dye pollutions from aqueous solutions: synthesis and characterization. Mater. Chem. Horizons 1 (1), 23–34. https://doi.org/10.22128/MCH.2022.544.1003.

Men, J.Y., Shi, H.X., Dong, C.Y., Yang, Y.Y., Han, Y.R., Wang, R.X., Zhang, Y.Q., Zhao, T., Li, J., 2021. Preparation of poly(sodium 4-styrene sulfonate) grafted magnetic chitosan microspheres for

adsorption of cationic dyes. Int. J. Biol. Macromol. 181, 810–823. https://doi.org/10.1016/j.ijbiomac.2021.04.079.

Mohammed, N., Grishkewich, N., Tam, K.C., 2018. Cellulose nanomaterials: promising sustainable nanomaterials for application in water/wastewater treatment processes. Environ. Sci. Nano. 3, 623–658. https://doi.org/10.1039/C7EN01029J.

Mu, Y.K., Du, H.X., He, W.Y., Ma, H.Z., 2022. Functionalized mesoporous magnetic biochar for methylene blue removal: performance assessment and mechanism exploration. Diam. Relat. Mater. 121,. https://doi.org/10.1016/j.diamond.2021.108795 108795.

Nnaji, P.C., Okolo, B.I., Onukwuli, O.D., 2020. Luffa cylindrica seed: biomass for wastewater treatment, sludge generation study at optimum conditions. Chem. Ind. Chem. Eng. Q. 26, 349–358. https://doi.org/10.2298/CICEQ190623012N.

Nnaji, P.C., Anadebe, V.C., Onukwuli, O.D., 2021. Potential of Luffa cylindrica seed as coagulation-flocculation (CF) agent for the treatment of dye wastewater: kinetic, mass transfer, optimization and CF adsorption studies. Arab. J. Chem. 15,. https://doi.org/10.1016/j.arabjc.2021.103629 103629.

Oun, A.A., Kamal, K.H., Farroh, K., Ali, E.F., Hassan, M.A., 2021. Development of fast and high-efficiency sponge-gourd fibers (Luffa cylindrica)/hydroxyapatite composites for removal of lead and methylene blue. Arab. J. Chem. 14,. https://doi.org/10.1016/j.arabjc.2021.103281 103281.

Sakhiya, A.K., Aier, I., Pathak, S., Anand, A., Jha, S., Vijay, V.K., Kaushal, P., 2021. Copper(II) removal from aqua solution using rice straw derived biochar. Mater. Today. 43, 740–745. https://doi.org/10.1016/j.matpr.2020.12.953.

Schio, R.R., Gonalves, J.O., Mallmann, E.S., Pinto, D., Dotto, G.L., 2021b. Development of a biosponge based on Luffa cylindrica and crosslinked chitosan for Allura red AC adsorption. Int. J. Biol. Macromol. 192, 1117–1122. https://doi.org/10.1016/j.ijbiomac.2021.10.096.

Schio, R.D.R., Martinello, B.D.K., Netto, M.S., Silva, L.L.O., Mallmann, E.S., Dotto, G.L., 2021a. Adsorption performance of Food Red 17 dye using an eco-friendly material based on Luffa cylindrica and chitosan. J. Mol. Liq. 349,. https://doi.org/10.1016/j.molliq.2021.118144 118144.

Shi, H.X., Dong, C.Y., Yang, Y.Y., Han, Y.R., Wang, F., Wang, C. X., Men, J.Y., 2020. Preparation of sulfonate chitosan microspheres and study on its adsorption properties for methylene blue. Int. J. Biol. Macromol. 163, 2334–2345. https://doi.org/10.1016/j.ijbiomac.2020.09.078.

Siddiqui, S.H., 2018. The removal of Cu^{2+}, Ni^{2+} and Methylene Blue (MB) from aqueous solution using Luffa Actangula Carbon: Kinetics, thermodynamic and isotherm and response methodology. Groundw. Sustain. Dev. 6, 141–149. https://doi.org/10.1016/j.gsd.2017.12.008.

Su, S.Z., Liu, Q., Liu, J.Y., Zhang, H.S., Li, R.M., Jing, X.Y., Wang, J., 2018a. Polyethyleneimine - functionalized Luffa cylindrica for efficient uranium extraction. J. Colloid Interf. Sci. 530, 538–546. https://doi.org/10.1016/j.jcis.2018.03.102.

Su, S.Z., Chen, R.R., Liu, Q., Liu, J.Y., Zhang, H.S., Li, R.M., Zhang, M.L., Liu, P.L., Wang, J., 2018b. High efficiency extraction of U (VI) from seawater by incorporation of polyethyleneimine, polyacrylic acid hydrogel and Luffa cylindrical fibers. Chem. Eng. J. 345, 526–535. https://doi.org/10.1016/j.cej.2018.03.164.

Tshikovhi, A., Mishra, S.B., Mishra, A.K., 2020. Nanocellulose-based composites for the removal of contaminants from wastewater. Int. J. Biol. Macromol. 152, 616–632. https://doi.org/10.1016/j.ijbiomac.2020.02.221.

Tunc, S., Duman, O., Gürkan, T., 2013. Monitoring the decolorization of acid orange 8 and acid red 44 from aqueous solution using fenton's reagents by online spectrophotometric method: effect of operation parameters and kinetic study. Ind. Eng. Chem. R. 52, 1414–1425. https://doi.org/10.1021/ie302126c.

Xu, B.C., Zheng, H.L., Zhou, H., Wang, Y.J., Luo, K., Zhao, C., Peng, Y., Zheng, X.Y., 2018. Adsorptive removal of anionic dyes by chitosan-based magnetic microspheres with pH-responsive properties. J. Mol. Liq. 256, 424–432. https://doi.org/10.1016/j.molliq.2018.02.061.

Zhang, Y.N., Guo, J.Z., Wu, C.Z., Huan, W.W., Chen, L., Li, B., 2022. Enhanced removal of Cr(VI) by cation functionalized bamboo hydrochar. Bioresource. Technol. 347,. https://doi.org/10.1016/j.biortech.2022.126703 126703.

Zhao, Y., Chen, T., Ma, R., Du, J.F., Xie, C., 2018. Synthesis of flower-like CeO_2/BiOCl heterostructures with enhanced ultraviolet light photocatalytic activity. Micro. Nano. Lett. 13, 1394–1398. https://doi.org/10.1049/mnl.2018.5228.

Zhao, Y., Yang, J.Y., Li, T.T., Liu, G., Wang, Y.Y., Jiang, Y., Wang, Z.X., Zhang, F.F., Li, Y.S., Liu, Y., 2021. Controlled preparation of a MCC-g-AM/EDA/PA loaded Fe(iii) adsorbent by the pre-radiation grafting method and its application for the adsorption removal of phosphate. RSC Adv. 11, 6173–6181. https://doi.org/10.1039/D0RA09389K.